

# Aligned Networks of Engineered Fibrillar Fibronectin Guide Cellular Orientation and Motility

Dylan B. Neale, Ayşe J. Muñiz, Michael S. Jones, Do Hoon Kim, Johanna M. Buschhaus, Brock A. Humphries, William Y. Wang, Brendon M. Baker, Jeffery E. Raymond, Luis Solorio, Gary D. Luker, and Joerg Lahann\*

The extracellular matrix (ECM) influences biological processes associated with tissue development and disease progression. However, robust cell-free techniques to control fiber alignment of naturally derived ECM proteins, such as fibronectin (Fn), remain elusive. It is demonstrated that controlled hydrodynamics of Fn solutions at the air/fluid interface of porous tessellated polymer scaffolds (TPSs) generates suspended 3D fibrillar networks with alignment across multiple length scales ( $<1$ ,  $1$ – $20$   $\mu\text{m}$ , extended to  $>1$  mm). The direction of the fluid flow and the architecture of the polymeric supports influence protein solution flow profiles and, subsequently, the alignment of insoluble Fn fibrils. Aligned networks of fibrillar Fn characteristically alter fibroblast phenotype, indicated by increased directional orientation, enhanced nuclear and cytoskeletal polarity, and highly anisotropic and persistent cell motility when compared with nonaligned 3D networks and 2D substrates. Engineered extracellular matrices (EECMs) establish a critically needed tool for both fundamental and applied cell biology studies, with potential applications in diverse areas such as cancer biology and regenerative medicine.

## 1. Introduction

The extracellular matrix (ECM) is a complex amalgam of biomacromolecules comprised of hundreds of proteins and glycans with tissue specific structural motifs. Central to tissue genesis, ECM composition and structure transform during healthy and pathobiological processes to characteristically impact function.<sup>[1–4]</sup> Aligned architecture is ubiquitous in ECM across various niches including soft tissue, skeletal muscle, cardiac tissue, and pathogenic tumor tissue.<sup>[5–8]</sup> On the macroscale, alignment guides load-bearing in tendons, facilitates force transmission in muscle, and promotes healthy cardiac processes,<sup>[4,7–9]</sup> while in cancer is correlated with poor prognosis.<sup>[10,11]</sup> In skin, local regions of anisotropic ECM fibers with long-range isotropy are characteristic of normal structure and mechanical stability,

whereas the deposition of dense, highly aligned ECM is associated with aberrant scar tissue.<sup>[12–14]</sup> On the cellular scale, ECM

D. B. Neale, D. H. Kim, Dr. J. E. Raymond  
Department of Chemical Engineering  
BioInterfaces Institute  
University of Michigan  
2800 Plymouth Road, Ann Arbor, MI 48109, USA

A. J. Muñiz, M. S. Jones  
Macromolecular Science and Engineering Program  
BioInterfaces Institute  
University of Michigan  
2800 Plymouth Road, Ann Arbor, MI 48109, USA


J. M. Buschhaus, W. Y. Wang, Prof. B. M. Baker  
Department of Biomedical Engineering  
University of Michigan  
Ann Arbor, MI 48109, USA

J. M. Buschhaus, Dr. B. A. Humphries  
Center for Molecular Imaging  
Department of Radiology  
BioInterfaces Institute  
University of Michigan  
109 Zina Pitcher Place, Ann Arbor, MI 48109, USA

Prof. L. Solorio  
Department of Biomedical Engineering  
Purdue University  
206 S Martin Jischke Drive, West Lafayette, IN 47907, USA

Dr. G. D. Luker  
Center for Molecular Imaging  
BioInterfaces Institute  
Department of Radiology  
Biomedical Engineering, and Microbiology and Immunology  
University of Michigan  
109 Zina Pitcher Place, Ann Arbor, MI 48109, USA

Prof. J. Lahann  
Director of the BioInterfaces Institute  
Departments of Chemical Engineering, Materials Science and Engineering, Biomedical Engineering, and the Macromolecular Science and Engineering Program  
University of Michigan  
NCRC B10-A175  
2800 Plymouth Road, Ann Arbor, MI 48109, USA  
E-mail: lahann@umich.edu

 The ORCID identification number(s) for the author(s) of this article can be found under <https://doi.org/10.1002/ssstr.202000137>.

DOI: 10.1002/ssstr.202000137

anisotropy has nuanced influences in wound healing, electrical signal propagation, angiogenesis, and remodeled pathogenic tissue,<sup>[15–20]</sup> where the complex origin–effect relationship of aligned ECM is just beginning to be understood using 2D culture models.<sup>[21]</sup> This manifests a need for engineered 3D protein structures with tunable alignment to serve as robust *in vitro* models and help elucidate the complex role of ECM organization.

Emerging studies into the architecture of ECM typically use synthetic materials, collagen gels, cell-secreted matrices or adsorbed protein layers deposited onto 2D substrates to model fibrillar structures.<sup>[22–26]</sup> Cell-secreted matrices model native fibrillar microenvironments, but these are complex amalgams of various deposited proteins and soluble factors.<sup>[27]</sup> Collagen gels are a prevalent biomaterial, where there exists several methods to create aligned networks *in vitro* including shear flow, magnetic fields, and mechanical strain.<sup>[23,28–32]</sup> Equivalent methods do not exist for other highly relevant ECM proteins, namely fibronectin (Fn). Fn is ubiquitous and indispensable for various processes in mammalian biology. It presents mostly as a large ( $\approx 440$  kDa) dimer in plasma and insoluble multimers in tissues.<sup>[33,34]</sup> Mounting evidence suggests that Fn has a significant role in governing cell orientation and motility.<sup>[25,26,34,35]</sup> In addition, cancer-associated fibroblasts secrete aligned Fn, among other macromolecules, which has been shown to promote the migratory behavior of tumor cells *in vitro*.<sup>[24,36]</sup>

Cell-mediated Fn fibrillogenesis is a complex process that primarily occurs through integrin binding of the solute dimeric protein followed by traction force-driven stretching that reveals conformationally active type III domains. These cryptic domains bind additional solute dimers via the 70 kDa N-terminus, leading to the formation of insoluble fibrillar networks.<sup>[37–39]</sup> Understanding the intricacies of native Fn assembly is a topic of ongoing investigation.<sup>[40–42]</sup> Despite its prevalence in mammalian biology, Fn's adoption as a 3D biomaterial has been limited, in part, due to the difficulty of understanding and controlling its assembly into insoluble fibrillar networks. Early work utilized solution-denaturants and reducing agents to assemble insoluble Fn materials.<sup>[43,44]</sup> Solution extraction combined with fluid-forces produced large, dense mats of oriented Fn via shearing through a syringe or on spinning impellers.<sup>[45–48]</sup> Recently, a solvent-based rotary spinning technique led to large-scale (centimeter-length), force-induced nanofiber Fn mats that were used in wound healing.<sup>[14]</sup> Material surfaces can also be used to promote the assembly of insoluble fibrils.<sup>[49–52]</sup> Notable examples include the demonstration of surface-detachable nanotextiles with precise control over  $x$ – $y$  plane arrangement but with limited thickness (1–10 nm).<sup>[51]</sup> Importantly, Fn adsorption onto surfaces does not necessarily promote assembly of Fn that facilitates binding of certain type III domains.<sup>[53]</sup> Forces generated from the expansion of lipid monolayers in contact with physiological buffers can be used to assemble Fn.<sup>[54]</sup> Other techniques utilize force at a liquid–air interface to promote assembly, where micron-scale Fn fibrils can be drawn out of concentrated Fn droplets.<sup>[45,55,56]</sup> Aggregation of Fn at the air–solution interface can be combined with droplet-shearing across microengineered surfaces to create suspended fibrils across small gap lengths ( $<10$   $\mu\text{m}$ ).<sup>[57,58]</sup> Critically, these techniques require manual manipulation to orient fibrils<sup>[45,55,56]</sup> with intrinsic length scale limitations that preclude formation of millimeter-length fibrillar networks with interconnected

3-dimensionality.<sup>[45,55–58]</sup> Recently, the creation of millimeter-scale suspended 3D fibrillar Fn networks compatible with conventional cell culture and analysis modalities were achieved,<sup>[53]</sup> however, they lacked precise control of fiber alignment.

Here, we demonstrate control over the degree of alignment of 3D fibrillar Fn networks suspended across porous polymer support structures without the use of solution denaturants or organic solvents. These engineered extracellular matrices (EECMs) display cell relevant 3-dimensionality ( $\approx 50$ – $70$   $\mu\text{m}$ ), suspension over large gap lengths (245–950  $\mu\text{m}$ ), and coverage over large areas ( $\approx 25$   $\text{mm}^2$ ). We further propose a process whereby fibril assembly at the air–solution interface is guided by flow profiles that can be tailored through physical interactions between the solution and polymeric support scaffold. This novel system is applied to study the influence of Fn fiber directionality on fibroblast morphology and motility. This work establishes a cell-free technique to model 3D fibrillar networks of Fn with controlled orientation using the purified protein. To our knowledge, this constitutes the first report of such a Fn-based system.

## 2. Results and Discussion

### 2.1. Polymer Scaffold Geometry and Orientation Induces Fibril Alignment During Hydrodynamically Induced Fibrillogenesis

We explored the hypothesis that tailored fluid-flow profiles across the tessellated polymer support structures at the air/fluid interface will influence directional orientation of the fibril architecture during hydrodynamically induced fibrillogenesis. Polymer scaffolds, comprised of SU-8, were engineered using photolithography to contain extended rectangular pores with varying gap lengths of  $248 \pm 3.2$   $\mu\text{m}$ ,  $497 \pm 5$   $\mu\text{m}$ , and  $946 \pm 2.6$   $\mu\text{m}$ , and with strut widths of  $36 \pm 0.7$   $\mu\text{m}$  (Table S1, Supporting Information). Scaffolds were engineered to be thin ( $112 \pm 1.7$   $\mu\text{m}$ ) to avoid limits in nutrient/oxygen diffusion, allow for efficient imaging, and provide sufficient free volume to be filled in by the suspended Fn networks ( $\approx 3.77$   $\text{mm}^3$ ). These rectangular pores ( $\approx 0.25/0.5/0.95$  mm by  $\approx 5.8$  mm) were tessellated across a length of  $\approx 5.8$  mm, and act as a highly porous, free-standing support structure for the suspended 3D fibrillar Fn networks. Although SU-8 is not a bioabsorbable polymer, it has been demonstrated to have *in vitro* and *in vivo* utility as a biomaterial.<sup>[59–61]</sup> Because of its simple processability via photolithography, it was used in this model system to allow for high fidelity to intended scaffold geometries, rapid fabrication, and mechanical robustness. Polymer scaffolds with pores of varying gap length are shown in scanning electron micrographs (SEMs) (Figure 1A, Table S1, Supporting Information). As shown in Figure 1B, the Fn networks are 3D fibrillar networks suspended across a highly porous scaffold comprised of tessellated rectangular pores. These scaffolds are herein referred to as tessellated polymer scaffolds (TPSs). Using fluid modeling (COMSOL Multiphysics), we compared the flow characteristics across TPSs with pores oriented perpendicular or parallel to the inlet flow direction; see Figure S1, Supporting Information, for a wireframe diagram to reference the scaffold geometry with respect to the flow direction. To inform the 3D model design, a two-phase, time-lapse 2D model was generated, (Figure S2, S3, Supporting Information). With perpendicularly

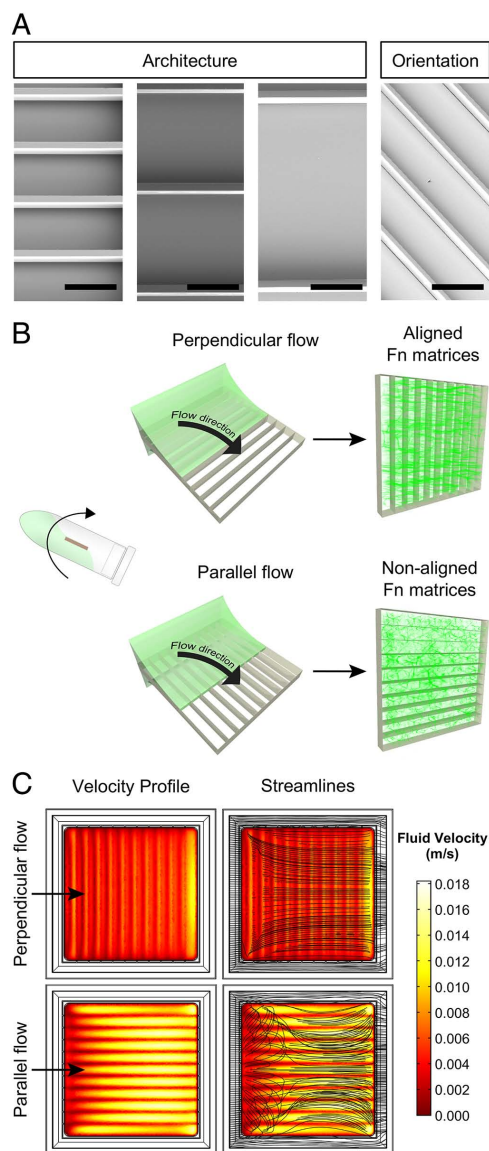


**Figure 1.** Polymer scaffold geometry and orientation induces fibril alignment during hydrodynamically induced fibrillogenesis. A) SEMs of TPSs with rectangular pore geometries made from SU-8 via photolithography. Scale bars (architecture) 250  $\mu\text{m}$ , (orientation) are 500  $\mu\text{m}$ . B) Illustration depicting how TPSs are coated via hydrodynamically induced fibrillogenesis to produce aligned or nonaligned 3D Fn matrices. C) Top-down view of COMSOL model revealing flow profiles when TPS pore direction is perpendicular or parallel to flow direction. Black arrows indicate the direction of fluid flow on the inlet side. Streamlines are shown in black and plotted over the velocity profile which is depicted via color from 0 to 0.018  $\text{m s}^{-1}$ .

orientated pores, the flow was slower and resulted in generally straighter streamlines across the entire length of the TPS (Figure 1C). The streamlines also exhibited a slightly periodic nature with some recombining flow profiles from pore to pore (Figure S4, Supporting Information). When the fluid-flow direction is parallel to the long axes of the pores, the flow tended to be faster with more vortices, which leads to warped streamlines across the length of the entire scaffold (Figure 1C, Figure S4,

Supporting Information). The modeling suggests that TPSs with perpendicularly oriented pores lead to a more coherently aligned fluid-flow field across the length of the scaffold. Collectively, the modeling data suggest fluid-flow profiles can be guided during hydrodynamically induced fibrillogenesis as a function of interactions between the supporting TPS and the protein solution. If fibril assembly follows fluid-flow profiles, hydrodynamically induced fibrillogenesis perpendicular to the long axis of the TPS pores would give rise to aligned Fn fibril architecture, represented schematically in Figure 1B. Conversely, if the fluid is directed such that the flow is parallel to the long axis of the pores, the fibrillar networks would be more disorganized and less oriented (Figure 1B). Throughout this article, alignment refers to individual fibrils within a network of Fn that share a common directionality axis, where the axis of alignment is defined as the  $0^\circ$ – $180^\circ$  horizontal line. In aligned engineered extracellular matrices (aEECM), the fibrils share a directional axis, whereas significantly fewer of the fibrils in nonaligned engineered extracellular matrices (naEECM) share a common axis and lack overall organization.

## 2.2. Precisely Aligned 3D Fn Networks Across the Tissue Length Scales

TPSs were coated with Fn at a concentration of 111  $\mu\text{g mL}^{-1}$  via rotation at 8 rpm (rotations per minute) following the procedure schematically represented in Figure 1B, described in the Experimental Section and previously reported.<sup>[53]</sup> With this technique, fibrillogenesis does not occur in the absence of fluid flow (i.e., 0 rpm).<sup>[53]</sup> We postulate the mechanism of fibril assembly occurs by a force-induced process at the solution/air interface across the TPS, which is likely similar to the fiber drawing/droplet shearing processes previously reported.<sup>[45,55,57]</sup> In addition, these fibrillar Fn materials are insoluble to an overnight treatment in 1% deoxycholate, further indicating that they are assembled, multimeric Fn networks.<sup>[53]</sup> SEMs of the TPS pores are overlaid in the upper right-hand corner of the maximum intensity projections (MIPs) to indicate the orientation of the TPS pores at the time of hydrodynamically induced fibrillogenesis with respect to the  $0^\circ$  fluid-flow direction (Figure 2A,B). These MIPs, captured via confocal laser scanning microscopy (CLSM), demonstrate that when TPS pores were oriented with the long axis perpendicular to the flow direction, the resultant Fn matrices were highly aligned (aEECMs), as confirmed by CLSM MIPs shown in Figure 2A. Given the large area of the scaffolds ( $\approx 5.8 \text{ mm} \times \approx 5.8 \text{ mm}$ ) and relatively small scaffold height ( $\approx 0.11 \text{ mm}$ ), the resulting suspended Fn matrices' directional orientation (aligned or non-aligned) was predominantly observed in the  $x$ - $y$  plane and not along the  $z$ -axis planes. Throughout the article, MIPs of confocal images are used for display purposes. To elucidate the 3-dimensionality at the cellular-length scale, both a volume render of an EECM (Figure 2) and a confocal image with an MIP in the center and orthogonal views along the  $z$ -axis planes are provided to demonstrate  $\approx 50$ – $70 \mu\text{m}$  of fibrillar Fn EECM depth, where Figure S5, Supporting Information, also demonstrates an EECM with cells integrating throughout the volume. These images demonstrate the EECMs are a relatively porous collection of interconnected fibrillar elements with cell-relevant 3-dimensionality.

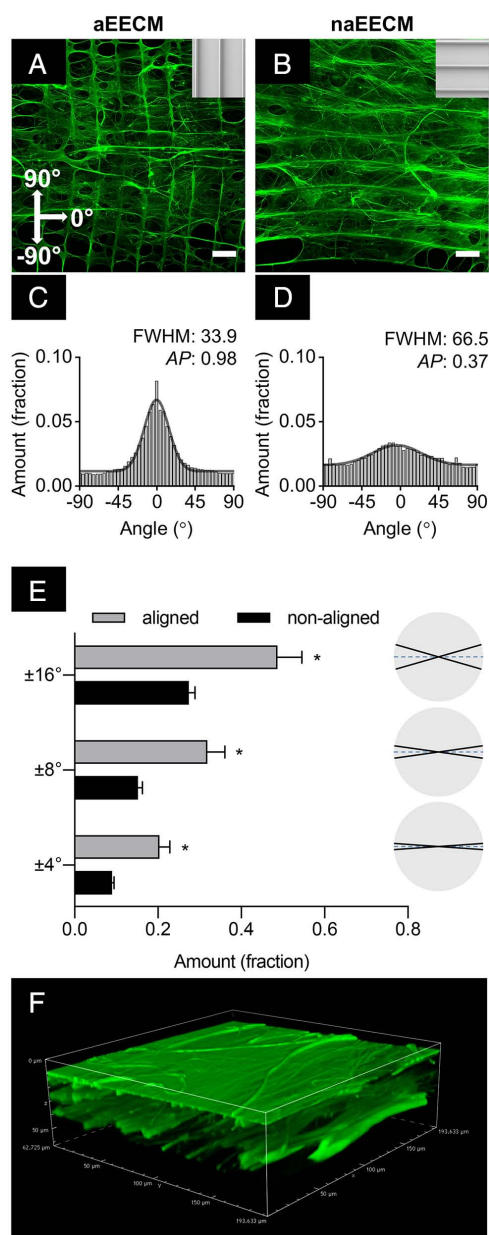


**Figure 2.** Precisely aligned 3D Fn networks across the tissue length scale. A,B) CLSM MIPs with SEMs of polymer scaffolds overlaid in the upper right-hand corner to illustrate the orientation of polymer pores with respect the 0° flow direction. Left column: aEECM. Right column: naEECM. Scale bars are 500 μm. C,D) Directionality histograms of CLSM MIPs for aEECM and naEECM, respectively. Gaussian fits are overlaid in black. FWHM are reported to indicate narrowness of the distribution, as well as an AP which indicates increases in aligned fibrils with higher values. E) Summation analysis of histogram data from C,D to assess the amount of features within different angle bins. The circular diagrams to the right of the graph graphically represent the boundaries of the bin (black lines), and the 0°–180° line (dashed blue line). F) Volume render of an aEECM (two coatings). The volume boundaries in the image are 193.633 μm (x,y) and 62.725 μm (z). The Holm–Sidak Multiple t-test was used to assess significance. \* $P \leq 0.05$ , \*\* $P \leq 0.01$ , \*\*\* $P \leq 0.001$ .

This is markedly different from other technologies used in this space, which are often gel-based systems that encapsulate and physically constrain cells within a volume of material.<sup>[62]</sup> Given the wide range of mammalian cell size ( $\approx 10$ – $100 \mu\text{m}$  in diameter), as well as tissue length scales ( $\approx 100 \mu\text{m}$  to cm), Figure S6, Supporting Information, defines the relative “tissue,” “cellular,” and “subcellular” length scales when describing features and elements used in this article.

COMSOL modeling predicted that at an inlet velocity of  $0.15 \text{ m s}^{-1}$ , lower gap lengths would lead to higher fluidic alignment (Figure S7A,B, Supporting Information). Optimal gap length is likely a tradeoff between ideal flow conditions and Fn’s proclivity to self-assemble and align over that length. Our model was designed to investigate the former, and thus it is expected that optimal experimental conditions would deviate based on Fn’s self-assembly.

Critically, as gap length (pore size) decreases, porosity also decreases. A  $500 \mu\text{m}$  gap length was chosen for the following studies because it led to highly aligned EECMs, with a higher porosity ( $\approx 94\%$ ) compared with the  $245 \mu\text{m}$  gap length ( $\approx 88\%$ ) (Table S1, Supporting Information), indicating a minimization of the amount of synthetic material present in the composite structure post-fibrillogenesis. In addition, aEECMs produced from gap lengths of  $950 \mu\text{m}$  were less aligned compared with  $500 \mu\text{m}$  gap lengths, demonstrated qualitatively by CLSM MIPs and reflected in the modeling data (Figure 2A,B; S7A,B; S8C,D, Supporting Information). In Figure 2C,D, the orientation of fibrils and larger fibrillar bundles was assessed along the tissue length scale via large regions of interests (ROIs). These data represent the orientation of fibrils around the axis of alignment (0°), where the y-axis displays the normalized power spectra resulting from a fast Fourier transform (FFT). This spectrum represents a convolution of both the number and intensity of the assessed fibers (Figure 2C,D). Gaussian distributions were fit to the data and the full width at half maximum values (FWHM) indicate narrowness of the distributions. In addition, the area underneath the Gaussian curve was normalized by the area underneath the y-offset to define an alignment parameter (AP), wherein a higher value represents a higher degree of fibril alignment; see Figure S9, Supporting Information. For TPSs with a  $500 \mu\text{m}$  gap length and pores oriented parallel to fluid flow (0°), naEECMs were formed as demonstrated qualitatively (Figure 2B), whereas when TPS pores were perpendicular to flow (90°), fibrils were more highly aligned (Figure 2A). Quantitative analysis revealed a FWHM of 66.5 and an AP of 0.37 (Figure 2D) for naEECM, compared with a FWHM of 33.9 and an AP of 0.98 in the aEECM group (Figure 2C). Additional analysis of the directionality data (Figure 2C,D) presents the summation of feature intensity of the normalized power spectra in directionality bins ( $\pm 4^\circ$ ,  $\pm 8^\circ$ ,  $\pm 16^\circ$ ) for aEECMs compared with naEECMs (shown in Figure 2E). Expanded data with higher bins are reported in Figure S10, Supporting Information. The directionality groups are represented graphically to the right of the figure for each respective subset. This analysis reveals that 20.4% of continuous features in the aEECMs fall into the narrow group of  $\pm 4^\circ$  around the axis of alignment, compared with only 8.9% in the naEECMs. In addition, nearly half of assessed features in aEECMs (48.6%)

fall within the  $\pm 16^\circ$ , compared with 27.4% in the naEECMs. Differences in means between naEECMs and aEECMs at  $\leq \pm 33^\circ$ , shown in Figure 2E, S10A, Supporting Information, were statistically significant. The differences observed at  $> \pm 33^\circ$  were not statistically significant. This analysis further elucidates that pore architecture during the coating process influences the flow profiles, and subsequently the orientation of the insoluble Fn fibrils. Higher-magnification SEMs confirm the presence of submicron fibrillar elements, as well as their aligned directional orientation at this length scale (Figure S6, Supporting Information). This also points toward a probable likelihood of EECMs inducing topographically mediated cell-phenomena.

These EECMs are suspended across large gap lengths (245–950  $\mu\text{m}$ ) that span multiple millimeters, as shown in Figure 2A,B, which is achieved using aqueous buffers and does not rely on the use of solution denaturants or solvents.<sup>[14,43–47]</sup> This marks an improvement over past reports of oriented fibrils across  $\approx 4 \mu\text{m}$  gap lengths.<sup>[57,58]</sup> In addition, these EECM constructs are a robust free-standing composite material that is easily handleable. Table S2, Supporting Information, overviews the characteristics of other fibrillar Fn biomaterials, as they compare with EECMs. The ROIs for directionality analysis at the tissue length scale are large, see Experimental Section. Importantly, the perceived degree of alignment of an interconnected fibrillar network can be impacted by the length scale of observation, where areas larger than the length of entanglements appear more randomly oriented.<sup>[62]</sup>

Collectively, these data demonstrate that control over the polymer-Fn solution fluid interface enables a precise, cell-free method to create engineered fibrillar Fn networks with controlled fibrillar alignment of subcellular features to larger fibrillar elements across the several millimeters.

### 2.3. Aligned Fn Networks Influence Fibroblast Orientation and Polarity

To evaluate the topographical impact of the EECMs at the cellular length scale, CLSM imaging of individual cells was performed at higher magnification. To evaluate changes in contact guidance in response to the topography of the Fn EECM, NIH-3T3 fibroblasts were cultured for 24 h. F-actin staining revealed fibroblasts cultured on the aEECMs were more elongated compared with naEECMs (Figure 3A,D). Analysis of cell directionality based on the F-actin staining at the cellular length scale reveals a similar FWHM (49.4) on aEECMs (Figure 3B) compared to the naEECMs (FWHM 49.7) Figure 3E; however, the AP values were separated by a tenfold margin: 0.80 and 0.08. Additional summation of the features of the F-actin directionality of cells seeded on aEECMs (Figure 3G), revealed 19.4% within  $\pm 8^\circ$  of the directionality axis, and 35.3% within  $\pm 16^\circ$ , compared with 11.3% and 21.2% for those cells seeded on naEECMs, respectively. Mirroring the analysis on the Fn networks, significantly higher amounts of F-actin features  $\leq \pm 16^\circ$  for cells seeded on aEECMs compared with naEECMs (Figure S10B, Supporting Information). The CLSM MIPs shown in Figure 3A,D confirm an excellent correlation between fibrillar alignment and cell directionality for aEECMs. In addition, the aspect ratios of both cell nuclei and their

cytoskeletons significantly increased when seeded on aEECMs compared with naEECMs Figure 3C,F. F-actin channels of CLSM MIPs were analyzed using a previously published MATLAB script to identify and quantify the presence of actin stress fibers (SFs), where representative analysis images are shown in Figure S11, Supporting Information.<sup>[63]</sup> A significantly higher number of SFs was observed in cells seeded on naEECMs (Figure 3H), which may indicate that cells seeded on aEECMs are migrating more than those seeded on naEECMs. Evidence suggests SFs are more prominent and in higher number in stationary cells, as migrating cells have to continuously break and reform their adhesions sites.<sup>[64,65]</sup> To further characterize EECMs at the cellular length scale, fibril diameters (Figure S12, Supporting Information) of the Fn channel of CLSM images were assessed using a previously published open-source software (GTFiber2, GitHub).<sup>[66]</sup> Examples of segmented images are provided in Figure S13, Supporting Information. These data revealed very similar, right-skewed distributions for both aEECMs and naEECMs with a mean of 4.3 and 4.1  $\mu\text{m}$ , respectively. The range between the  $-1$  standard deviation and the  $+1$  standard deviation was 2.4–7.5  $\mu\text{m}$  for aEECM and 2.3–7.2  $\mu\text{m}$  for naEECM.

To determine whether EECM topography impacts cell growth, proliferation on aEECMs and naEECMs was assessed over 6.5 days. The rate of proliferation was very similar and not significantly different for all time points, Figure S14, Supporting Information. Cell saturation on the EECMs occurred at 5.5 days, where  $360\,000 \pm 62\,000$  and  $391\,000 \pm 13\,000$  cells were estimated on naEECMs and aEECMs, respectively. Furthermore, EECMs are remarkably stable in cell culture conditions, as shown by imaging of an aEECM over 4 days of cell culture (Figure S15, Supporting Information). Figure S15, Supporting Information, indicates no appreciable differences in the fibrillar Fn network integrity despite nearly complete cell coverage, which is displayed in the differential interference contrast (DIC) counter image.

Collectively, the data presented in Figure 3 support the notion that fibroblasts respond to the topography of EECMs, wherein fibril alignment does not impact proliferation rate, but over short periods of time causes a significant increase in cell alignment, an increase in cytoskeletal/nuclear elongation, as well as a decrease in actin SFs. Recent work where Fn was adsorbed onto a 2D surface using microcontact printing, revealed that alignment of contact printed lines of solute Fn had a substantial impact on cell morphology, polarization, and migration.<sup>[25]</sup> In 3D fibrillar Fn networks, alignment also substantially impacted the polarization and orientation of cells.

### 2.4. Aligned Fn Guides Fibroblast Motility

To further elucidate the influence of Fn architecture on fibroblast motility, time-lapse microscopy studies were performed. To quantify cell motility in 3D suspended Fn EECMs, time-lapse fluorescent microscopy was performed on NIH-3T3 fibroblasts containing a H2B-RFP nuclear reporter in an incubator chamber over 20 h with 20 min imaging intervals. Spontaneous migration occurs on EECMs of different topographical alignment in the absence of chemotactic gradients and other external cues. The data generated from the nuclei tracking analysis were then fit to the anisotropic persistent random walk (APRW) model

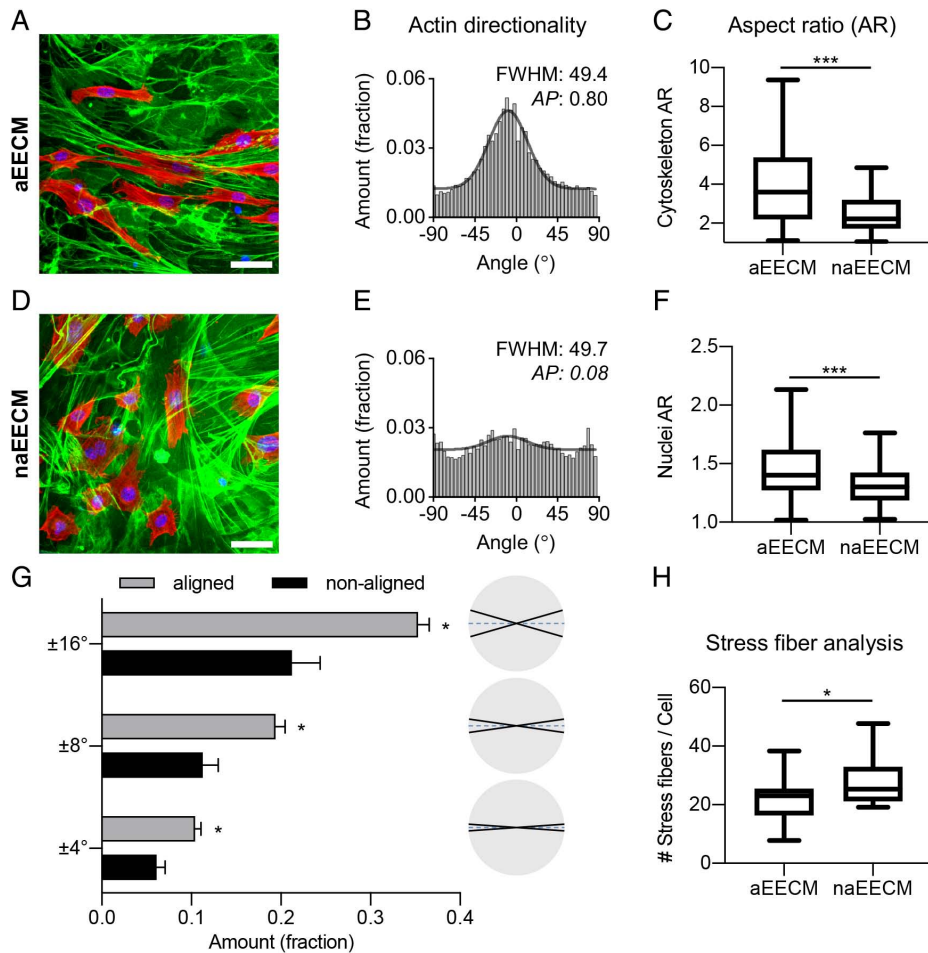


**Figure 3.** Aligned Fn networks influence fibroblast orientation and polarity on the cellular length scale. NIH-3T3s align with Fn fibrils on aEECM significantly compared with naEECM. A,D) Confocal MIPs of NIH-3T3s. Green: Fn, red: F-actin, blue: nuclei. A gamma correction of 0.5 was applied to the actin channel for visualization purposes. Scale bars: 50  $\mu\text{m}$ . B,E) Actin directionality analysis histograms. Gaussian fits are overlaid in black. FWHM are reported to indicate narrowness of the distribution, as well an AP which indicates increases in aligned fibrils with higher values. C,F) Aspect ratio analysis of actin morphology and nuclear morphology, respectively. G) Binning analysis of histogram data from B,E to assess the fraction of the fibrils falling within different angle bins. The circular diagrams to the right of the graph graphically represent the boundaries of the bin (black lines), and the  $0^\circ$ – $180^\circ$  line (dashed blue line). H) Actin SF analysis of F-actin images displays the number of SFs per cell in the y-axis. The Mann–Whitney U and Holm–Sidak Multiple t-test were performed to compare groups and assess statistical significance. \* $P \leq 0.05$ , \*\* $P \leq 0.01$ , \*\*\* $P \leq 0.001$ .

published by Wu et al. to quantify metrics of anisotropic index, persistence time and speed in the primary (p) and nonprimary (np) directions.<sup>[67]</sup> Qualitatively, cells migrated straighter and displaced further on aEECMs as seen in representative images of migration tracks overlaid on a bright-field image of the initial frame (Figure 4A,D,G). The wind-rose plots shown in Figure 4B,E,H quantitatively indicate that a larger population of migratory cells displaced in the direction of the axis of alignment ( $0^\circ$ – $180^\circ$  line). These findings are corroborated by cell tracks plotted as walk plots (Figure 4C,F,I). Critically, the metrics generated via the APRW model suggest a significant increase in directionally persistent cell migration on aEECMs compared with naEECMs and 2D control substrates (Figure 4J,K). Both persistence time and anisotropic migration were increased in the 3D system compared with 2D, confirming findings by Wu et al. and underlining the importance of studying cell phenomena such as directionally persistent cell migration in 3D systems.<sup>[68]</sup> As

expected, most of the cells on 2D surfaces had lower persistence time with a third quartile value of 37 min ( $\approx 2$  intervals) for the distribution (Figure 4J). In stark contrast, also shown in Figure 4J, persistence times of cells seeded on naEECMs revealed a third quartile of 111 min ( $\approx 5.5$  intervals) while the third quartile of the persistence time distribution of cells seeded on aEECMs was 177 min ( $\approx 9$  intervals) (Figure 4J). The distinct differences in fibroblast motility on 2D substrates, naEECMs, and aEECMs are also reflected in the anisotropic indices of the primary cell direction, where the third quartiles were 5.1, 20.6, and 60.7, respectively (Figure 4K). The anisotropic index values on aEECMs are substantially higher than a previous report of primary mouse fibroblasts assessed in a 2D scratch wound assay, which was 2.4.<sup>[69]</sup> Values of speed were higher on 2D compared with 3D, Figure 4L, which is consistent with reports from Wu et al. Interestingly, cell speed was not significantly different between aEECM and naEECM, Figure 4L. Although studies of

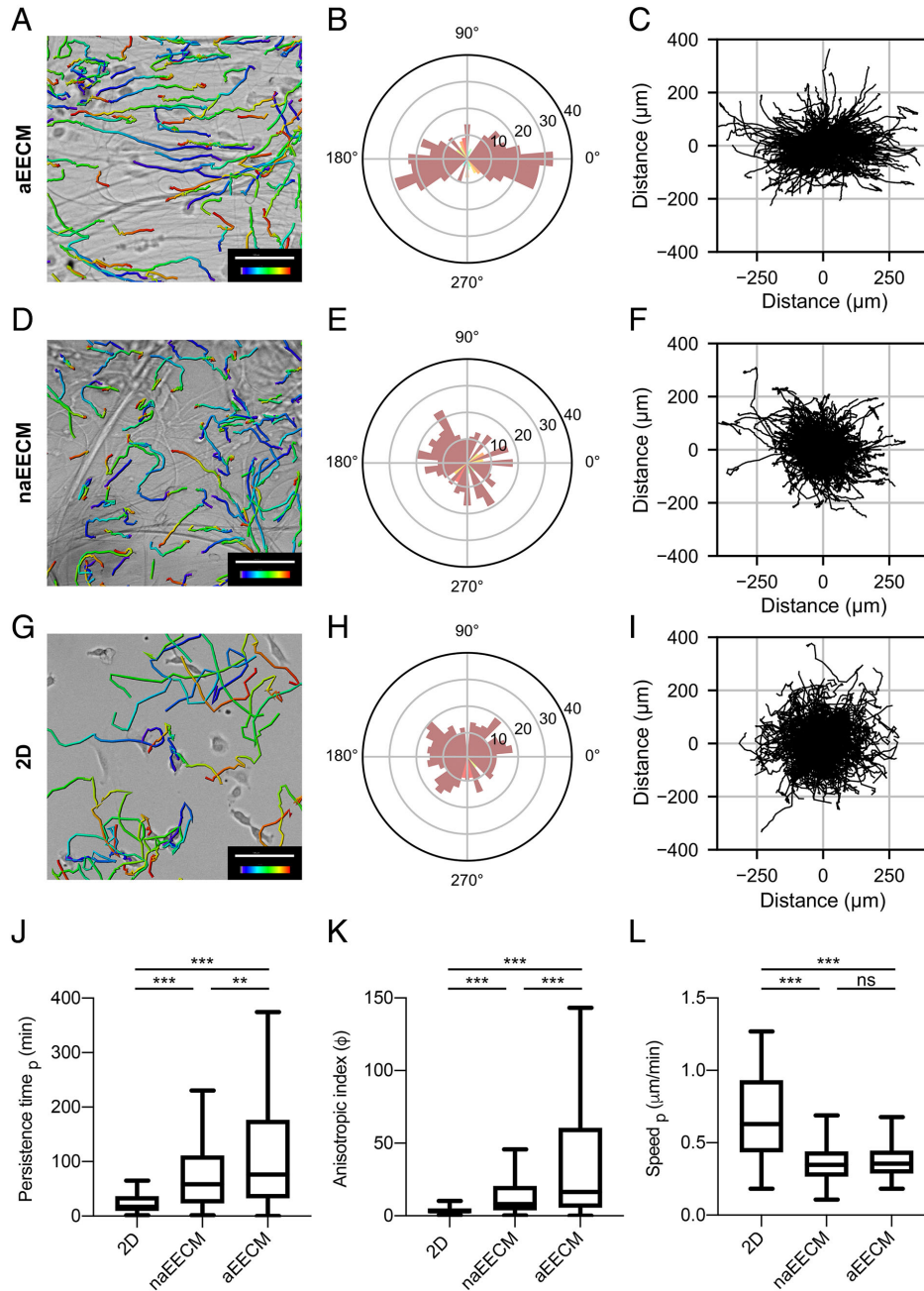


**Figure 4.** Aligned Fn guides fibroblast motility. Live cell migration analysis on A–C) aEECM, D–F) naEECM, and G–I) 2D, which reveals significant directionally persistent migration along aligned fibrils compared with nonaligned fibrils and 2D. A, D, G) Representative cell track images are overlaid onto bright-field images ( $t = 0$ ). Scale bars = 100  $\mu\text{m}$ . The time reference bar indicates increasing time from blue to red. B, E, H) Wind rose plots display the number of cells (length of bar from the origin) and their respective direction from  $0^\circ$  to  $360^\circ$  in  $10^\circ$  bins. C, F, I) Walk plots displaying individual cell paths from their origin as a function of distance in the  $x$ - $y$  directions. J) Box plot of cell persistence time assessed in the primary direction, extracted from the APRW model. K) Box plot of cell movement anisotropic index data was calculated from persistence time and speed. L) Box plot of cell speed, as determined from the APRW model. The Kruskal–Wallis test and post-hoc analysis via a Dunn’s multiple comparisons test were performed to assess statistical significance.  $*P \leq 0.05$ ,  $**P \leq 0.01$ ,  $***P \leq 0.001$ .

cell-secreted matrices point to Fn as a key player in anisotropic cell migration, the findings in this article demonstrate the ability to model these migratory phenomena and point to aligned fibrillar Fn as a driver of directionally persistent cell migration.

To evaluate suitability of EECMs to be applied in other biological contexts, a proof-of-concept study was performed to assess the attachment and/or expansion of pluripotent stem cells and breast cancer cell lines, Figure S16, Supporting Information. EECMs

facilitated the attachment, rapid flattening, and expansion of human embryonic stem cell colonies, as well as the attachment of single induced pluripotent stem cells (iPSCs) that were reliably expanded to confluence over 14 days. Furthermore, EECMs facilitate the attachment and growth of various cancer cell lines (MDA-MB-231s, SUM-159s, MCF7s) Figure S16, S5, Supporting Information, as well as primary patient tumor cells.<sup>[53]</sup>

Cell migration processes are critical in embryogenesis, wound healing, as well as cancer metastasis,<sup>[70,71]</sup> but are inherently different in 3D environments compared with 2D due to the fact that cells access environmentally mediated motility modes.<sup>[62,72]</sup> Although anisotropic cell migration induced from chemotactic and mechanical gradients has been well studied, topographically mediated migration is less understood and predominately studied in engineered 2D systems.<sup>[73–75]</sup> Using adsorbed Fn on 2D surfaces, certain domains have been implicated in directing persistent cell migration,<sup>[26,35]</sup> whereas our findings underscore alignment of Fn networks as a major factor of directionally persistent migration in the absence of other known external cues.

Considering the importance of directional motility in wound healing, embryogenesis, as well as tumor progression, these Fn EECMs provide a novel 3D platform for future studies to better understand the role Fn has in governing cell migration in various tissue contexts.

### 3. Conclusion

Controlled hydrodynamics of a Fn solution over TPSs induces protein fibrillogenesis, wherein alignment of 3D fibrillar Fn networks can be modulated by engineering the direction of the fluid profiles, in the absence of solution denaturants or solvents. Collectively, these data demonstrate Fn fibril alignment as a major ECM factor in directing cell orientation, where engineered fibrillar Fn networks induce fibroblast polarity and serve as contact guidance “highways” that cause a dramatic increase in directionally persistent motility. Building on previous literature in 2D model systems, these results were gathered using a 3D in vitro system composed of purified Fn. Although engineered 2D and 2.5D systems provide remarkable control over the presentation of topographical information for studying cell migration, in tissues the role of ECM topography is inextricably linked to composition. Hence, 3D protein-based in vitro models offer an attractive option for decoupling these matrix properties; however, controlling the assembly and structure of proteinaceous materials is a significant challenge where oriented EECMs constitute an advancement. This is especially important in the context of Fn because it is a known mechanosensitive protein with conformationally active binding domains, and future work would benefit from utilizing EECMs to decouple Fn-specific cues.

The potential utility of these constructs in tissue engineering is widespread given they are easily handleable, well-plate compatible, porous, optically translucent, and compositionally defined. Their open architecture allows for efficient cell seeding, recovery, and imaging. These characteristics make them compatible with many conventional cell analysis and imaging modalities as is demonstrated in this article as well as our previous work.<sup>[53]</sup> Future work would benefit from extending the concepts outlined in this article to create aligned Fn matrices with biodegradable

polymers via the utilization of advanced 3D printing techniques such as 3D jet-writing or melt-electrospinning as the supporting scaffold to access in vivo application spaces.<sup>[76,77]</sup>

This novel technology provides a critical link between biologically derived and synthetic biomaterials and will enable a broad range of studies on ECM-driven cell phenomena in aligned matrices. With further work, these hydrodynamically-induced fibrillar networks may lead to novel in vitro models for studying ECM-mediated phenomena in healthy and diseased tissue states.

### 4. Experimental Section

**Materials:** Polymer scaffolds were made of SU-8 2050 (Kayaku Advanced Materials, Westborough, MA, USA) using a photolithography lift-off procedure described previously.<sup>[60,78]</sup> Briefly, three layers of OmniCoat (Kayaku Advanced Materials, Westborough, MA, USA) were spun onto 4-in. silicon wafers and transferred to a hot plate at 200 °C for 1 min after each coating. SU-8 2050 was spun to the desired thickness, allowed to degas overnight, before UV curing per the manufacturer’s recommendations. Following lift-off in SU-8 developer (Kayaku Advanced Materials, Westborough, MA, USA), scaffolds were extensively rinsed (7–10 times) with fresh isopropyl alcohol and allowed to dry for at least 1 week before use in cell culture. SU-8 scaffolds were then attached to custom stainless-steel frames before applying the protein coating.

**Protein Coating:** Polymer scaffolds were coated with human Fn (Corning Inc, Corning, NY) that was diluted to a concentration of 111  $\mu\text{g mL}^{-1}$  in calcium/magnesium free Dulbecco’s phosphate buffered saline (DPBS) for 2 h, as described previously.<sup>[53]</sup> Briefly, TPSs were suspended with the center of the scaffold at the solution/air interface, and with the steel-frame/scaffold construct centered on the long-axis of a low-binding microcentrifuge tube (Biotix, San Diego, CA, USA). The TPSs were then gently sheared in an Eberbach EL655.1 Incubator tumbler (Eberbach Corp., Belleville, MI, USA) at 8 rpm and 30 °C.

**Fluid-Flow Modeling:** COMSOL 5.3a was used to simulate fluid flow during the Fn coating process. Solidworks 2018 SP 4.0 was used to create a dimensionally accurate CAD model of the SU-8 scaffolds mounted on a frame with a cuboidal inlet/outlet (with a cross-sectional area matching that of the centrifuge tube) underneath the scaffold shown in Figure S1, Supporting Information. The polymer scaffold was drawn dimensionally accurate: the struts were 35  $\mu\text{m}$  wide with gap lengths of 245, 500, and 950  $\mu\text{m}$ . The 3D model was approximated as steady state, laminar flow. The SU-8 polymer was modeled as nylon and the dilute Fn solution as water from COMSOL’s material library. The scaffold material was treated as a no-slip boundary, and the air–liquid interface was treated as a slip-boundary. A separate, 2D, time-dependent COMSOL model consisting of an air and liquid phase in a tube (geometrically similar to the microcentrifuge tube used for the hydrodynamically induced coating), at an angular velocity of 8 rpm was used and to elucidate the velocity at the inlet of the 3D model, Figure S2,3, Supporting Information. Based on this 2D model, an inlet velocity of 0.15  $\text{m s}^{-1}$  was used in the 3D model. COMSOL’s streamlines and velocity slice analysis functions were used to create the plots of flow behaviors around the scaffolds shown throughout the article.

**Cell Culture:** NIH-3T3s were cultured in high-glucose Dulbecco’s Modified Eagle Medium (DMEM) supplemented with 10% (v/v) fetal bovine serum (FBS) and 1% (v/v) antibiotic–antimycotic (ThermoFisher Scientific, Waltham, MA, USA). Cells were tested and confirmed negative for mycoplasma before studies were performed using a Lonza MycoAlert kit (Lonza, Basel, Switzerland) in accordance with the manufacturer recommendations.

**Cell Elongation Imaging:** 100 000 unlabeled NIH-3T3 fibroblasts were seeded on the aligned versus nonaligned Fn matrices in a 100  $\mu\text{L}$  droplet for 1 h at 37 °C in an ultralow adhesion 24-well plate (Corning Inc, Corning, NY, USA). They were then topped off with 1 mL of fresh culture medium and allowed to spread for 24 h. They were then fixed overnight at room temperature in 4% paraformaldehyde, then washed three times with DPBS and



prepared for staining. Cytoskeleton aspect ratio values represent the cell length divided by cell width. Nuclear aspect ratio values were generated using ImageJ to fit an ellipse and were the long axis divided by the short axis. EECMs (aligned versus nonaligned) were produced in triplicate. 7 ROIs within each EECM was assessed for a total of 42 multichannel images.

**Cell Proliferation Assay:** 100 000 NIH-3T3s were seeded in 1 mL of complete media on EECMs. A resazurin-based assay, Tox8 (Sigma-Aldrich, St. Louis, MO, USA), was used to assess metabolic activity. Cells were incubated with 10% (v/v) Tox8 reagent in complete media for 1 h. The supernatant was removed, spun at  $800 \times g$  for 5 min to pellet any potential detached cells, and the fluorescent intensity was measured (excitation 560 nm, emission 590 nm) using a Molecular Devices SpectraMax M5e plate reader (Molecular Devices, LLC, San Jose, CA). Measurements were normalized to the initial timepoint at 13.5 h. To estimate the cell number on the scaffolds, a serial dilution of a known number of cells were seeded onto 24-well plates, allowed to attach for 5 h, then treated with the same Tox8 protocol. A simple linear regression was fit to the data ( $R^2 = 0.9938$ ) to correlate the fluorescence intensity values to cell number using Graphpad Prism (v 8.4.3, San Diego, CA, USA).

**Fluorescence Staining:** To visualize the Fn for directionality analysis, unmodified Fn was blended with Dylight-650 conjugated Fn (5.6% v/v). The dye used was an NHS-ester DyLight-650 and was prepared in accordance with manufacturer recommendations (ThermoFisher Scientific, Waltham, MA, USA). In the cell spreading assay, nuclei were stained with Hoechst 33 342 (ThermoFisher Scientific, Waltham, MA, USA), and actin with Alexa Fluor 488 phalloidin (ThermoFisher Scientific, Waltham, MA, USA). The Fn matrices were stained with anti-Fn polyclonal antibody F3648 (Sigma-Aldrich, St. Louis, MO, USA).

**Live Cell Migration Assay:** NIH-3T3 were engineered with a H2B-RFP reporter to visualize the nuclei for live cell tracking. Images were taken using an Olympus-IX83 with a humidified live cell incubator, at a temperature of 37 °C with 5% CO<sub>2</sub>. Cells were seeded at 50 000 in 1 mL of complete media and allowed to attach for 1 h before acclimating to microscope incubator for 1 h and imaged for 20 h. Image sets were processed using Imaris (Bitplane, Belfast, UK) to render cell position over time by tracking cell nuclei. Each trace set was manually inspected to ensure the traces were accurately representing cell motility. Hence, given the imaging modality, the cell migration patterns were 2D projections of migration within the 3D EECMs. Data was then fit to the APRW model where persistence (P) and speed (S) along the primary (p) and nonprimary (np) directions was calculated on a single-cell basis.

**Directionality Analysis:** The directionality of both Fn fibrils across the tissue length scale and actin staining at the cellular length scale were analyzed using the Directionality plugin in Fiji (ImageJ) with the Fourier components method on CLSM MIPs. The “amount” represents the relative fraction of intensity in a given angle bin normalized by all the power spectrum intensity. Notably, with this methodology, intensity associated with the off-axis events include the width of well aligned features and should not be taken as a pure count of unaligned fiber (i.e., intensity is feature intensity-based, not count-based). When assessing Fn fibrils at the tissue length scale, 9–10 ROIs with an average size of  $\approx 1\,300\,000\ \mu\text{m}^2$  were chosen within SU-8 gap length across the length of the scaffold and accrued over three replicates. Using OriginPro (v. 2019, OriginLab Corp., Northampton, MA, USA), a Gaussian distribution was fit to the histograms and the FWHM values were reported as an indication of how wide or narrow the distributions were. In addition, an AP was defined as being the area under the Gaussian curve, normalized by the area under the y-offset. See Supporting Information for further details and Figure S9, Supporting Information, for a graphical representation.

**Statistics:** Three or more replicates were used to generate the data throughout the article unless otherwise noted. For statistical analyses, either custom Python script or Graphpad Prism (v 8.4.3, San Diego, CA, USA) were used. The Shapiro–Wilks Test was used to determine whether the data follow a normal distribution. Equal variance was assessed using Levene’s test. When comparing three or more groups, if the data are not normal or do not have equal variance between groups, then the Kruskal–Wallis H-test ( $n > 5$ ) followed by post-hoc analysis with the Dunn’s multiple comparisons test was performed to assess levels of

statistical significance among the groups. For comparing two groups, the Mann–Whitney U Test was performed if the data were nonparametric and a T-test if data were parametric or the Holm–Sidak Multiple t-test. Throughout the article:  $p \leq 0.05^*$ ,  $p \leq 0.01^{**}$ ,  $p \leq 0.001^{***}$ .

## Supporting Information

Supporting Information is available from the Wiley Online Library or from the author.

## Acknowledgements

This work was supported by the National Institute of Health under grant no. U01CA210152 R01CA238042, R01CA196018, R01CA238023, R33CA225549, R50CA221807, and R37CA222563, as well as the National Science Foundation under grant no. EEC-1647837 (Cell-Met). The authors also acknowledge personnel support from the National Institute of Health under grant no. T32 GM008353 (D.B.N.) and R00CA198929 (L.S.), as well as the National Science Foundation under grant no. DGE 1256260 (A.J.M.) and under grant no. DGE 1256260 (J.M.B.), and the American Cancer Society–Michigan Cancer Research Fund PF-18-236-01-CCG (B.A.H.). Eberbach Corporation, Belleville, MI generously donated the incubator tumbler used in these studies. The authors thank Soroush Moghadam from Ronald Larson’s lab at the University of Michigan for enlightening discussions regarding COMSOL modeling. The authors also thank Zackary Dodson from Thomas Downar’s lab at the University of Michigan for assistance in generating custom Python scripts.

## Conflict of Interest

The authors declare no conflict of interest.

## Data Availability Statement

The data that support the findings of this study are available from the corresponding author upon reasonable request.

## Keywords

alignment, cell motility, fibronectin, persistence, 3D cell culture

Received: November 20, 2020

Revised: January 17, 2021

Published online: March 1, 2021

- [1] C. Bonnans, J. Chou, Z. Werb, *Nat. Rev. Mol. Cell Biol.* **2014**, *15*, 786.
- [2] R. O. Hynes, A. Naba, *Cold Spring Harb. Perspect. Biol.* **2012**, *4*, a004903.
- [3] A. Steier, A. Muñiz, D. Neale, J. Lahann, *Adv. Mater.* **2019**, *31*, 1806898.
- [4] J. K. Mouw, G. Ou, V. M. Weaver, *Nat. Rev. Mol. Cell Biol.* **2014**, *15*, 771.
- [5] P. M. Wigmore, G. F. Dungleon, *Int. J. Dev. Biol.* **1998**, *42*, 117.
- [6] N. F. Huang, S. Patel, R. G. Thakar, J. Wu, B. S. Hsiao, B. Chu, R. J. Lee, S. Li, *Nano Lett.* **2006**, *6*, 537.
- [7] I. J. LeGrice, B. H. Smaill, L. Z. Chai, S. G. Edgar, J. B. Gavin, P. J. Hunter, *Am. J. Physiol. Circ. Physiol.* **1995**, *269*, H571.
- [8] M. O’Brien, in *Tendon Inj.* (Eds: N. Maffulli, P. Renström, W. B. Leadbetter), Springer-Verlag, London, **2005**, pp. 3–13.
- [9] R. L. Lieber, in *Skeletal Muscle Structure, Function, And Plasticity* (Ed: T. Julet), Lippincott Williams & Wilkins, Philadelphia, PA **2002**.

- [10] M. W. Conklin, J. C. Eickhoff, K. M. Ricking, C. A. Pehlke, K. W. Eliceiri, P. P. Provenzano, A. Friedl, P. J. Keely, *Am. J. Pathol.* **2011**, *178*, 1221.
- [11] P. P. Provenzano, K. W. Eliceiri, J. M. Campbell, D. R. Inman, J. G. White, P. J. Keely, *BMC Med.* **2006**, *4*, 38.
- [12] M. W. J. Ferguson, S. O'Kane, *Philos. Trans. R. Soc. B Biol. Sci.* **2004**, *359*, 839.
- [13] P. P. M. Van Zuijlen, J. J. B. Ruurda, H. A. Van Veen, J. Van Marle, A. J. M. Van Trier, F. Groenevelt, R. W. Kreis, E. Middelkoop, *Burns* **2003**, *29*, 423.
- [14] C. O. Chantre, P. H. Campbell, H. M. Golecki, A. T. Buganza, A. K. Capulli, L. F. Deravi, S. Dauth, S. P. Sheehy, J. A. Paten, K. Gledhill, Y. S. Doucet, H. E. Abaci, S. Ahn, B. D. Pope, J. W. Ruberti, S. P. Hoerstrup, A. M. Christiano, K. K. Parker, *Biomaterials* **2018**, *166*, 96.
- [15] K. D. Costa, E. J. Lee, J. W. Holmes, *Tissue Eng.* **2003**, *9*, 567.
- [16] K. Ronaldson-Bouchard, S. P. Ma, K. Yeager, T. Chen, L. Song, D. Sirabella, K. Morikawa, D. Teles, M. Yazawa, G. Vunjak-Novakovic, *Nature* **2018**, *556*, 239.
- [17] C.-Y. Chung, H. Bien, E. Entcheva, *J. Cardiovasc. Electrophysiol.* **2007**, *18*, 1323.
- [18] M. Basan, J. Elgeti, E. Hannezo, W.-J. Rappel, H. Levine, *Proc. Natl. Acad. Sci. USA* **2013**, *110*, 2452.
- [19] D. M. Gilkes, G. L. Semenza, D. Wirtz, *Nat. Rev. Cancer* **2014**, *14*, 430.
- [20] A. L. Bauer, T. L. Jackson, Y. Jiang, *PLoS Comput. Biol.* **2009**, *5*, e1000445.
- [21] D. Park, E. Wershof, S. Boeing, A. Labernadie, R. P. Jenkins, S. George, X. Trepap, P. A. Bates, E. Sahai, *Nat. Mater.* **2020**, *19*, 227.
- [22] A. Ray, O. Lee, Z. Win, R. M. Edwards, P. W. Alford, D.-H. Kim, P. P. Provenzano, *Nat. Commun.* **2017**, *8*, 14923.
- [23] J. Torbet, M. Malbouyres, N. Builles, V. Justin, M. Roulet, O. Damour, Å. Oldberg, F. Ruggiero, D. J. S. Hulmes, *Biomaterials* **2007**, *28*, 4268.
- [24] J. Stanisavljevic, J. Loubat-Casanovas, M. Herrera, T. Luque, R. Pena, A. Lluch, J. Albanell, F. Bonilla, A. Rovira, C. Pena, D. Navajas, F. Rojo, A. Garcia de Herreros, J. Baulida, *Cancer Res.* **2015**, *75*, 284.
- [25] W. Y. Wang, A. T. Pearson, M. L. Kutys, C. K. Choi, M. A. Wozniak, B. M. Baker, C. S. Chen, *APL Bioeng.* **2018**, *2*, 046107.
- [26] D. Missirlis, T. Haraszti, H. Kessler, J. P. Spatz, *Sci. Rep.* **2017**, *7*, 3711.
- [27] H. Ragelle, A. Naba, B. L. Larson, F. Zhou, M. Prijčić, C. A. Whittaker, A. Del Rosario, R. Langer, R. O. Hynes, D. G. Anderson, *Biomaterials* **2017**, *128*, 147.
- [28] K. M. Ricking, B. L. Cox, M. R. Salick, C. Pehlke, A. S. Ricking, S. M. Ponik, B. R. Bass, W. C. Crone, Y. Jiang, A. M. Weaver, K. W. Eliceiri, P. J. Keely, *Biophys. J.* **2014**, *107*, 2546.
- [29] C. Guo, L. J. Kaufman, *Biomaterials* **2007**, *28*, 1105.
- [30] N. Saeidi, E. A. Sander, J. W. Ruberti, *Biomaterials* **2009**, *30*, 6581.
- [31] B. Lanfer, U. Freudenberg, R. Zimmermann, D. Stamov, V. Körber, C. Werner, *Biomaterials* **2008**, *29*, 3888.
- [32] A. Ray, Z. M. Slama, R. K. Morford, S. A. Madden, P. P. Provenzano, *Biophys. J.* **2017**, *112*, 1023.
- [33] A. J. Zollinger, M. L. Smith, *Matrix Biol.* **2017**, *60–61*, 27.
- [34] C. Frantz, K. M. Stewart, V. M. Weaver, *J. Cell Sci.* **2010**, *123*, 4195.
- [35] D. Missirlis, T. Haraszti, C. V. C. Scheele, T. Wiegand, C. Diaz, S. Neubauer, F. Rechenmacher, H. Kessler, J. P. Spatz, *Sci. Rep.* **2016**, *6*, 23258.
- [36] B. Erdogan, M. Ao, L. M. White, A. L. Means, B. M. Brewer, L. Yang, M. K. Washington, C. Shi, O. E. Franco, A. M. Weaver, S. W. Hayward, D. Li, D. J. Webb, *J. Cell Biol.* **2017**, *216*, 3799.
- [37] Y. Mao, J. E. Schwarzbauer, *Matrix Biol.* **2005**, *24*, 389.
- [38] P. Singh, C. Carragher, J. E. Schwarzbauer, *Annu. Rev. Cell Dev. Biol.* **2010**, *26*, 397.
- [39] C. Wu, V. M. Keivenst, T. E. O'Toole, J. A. McDonald, M. H. Ginsberg, *Cell* **1995**, *83*, 715.
- [40] S. M. Früh, I. Schoen, J. Ries, V. Vogel, *Nat. Commun.* **2015**, *6*, 1.
- [41] C. A. Lemmon, S. H. Weinberg, *Sci. Rep.* **2017**, *7*, 18061.
- [42] J. A. Paten, C. L. Martin, J. T. Wanis, S. M. Siadat, A. M. Figueroa-Navedo, J. W. Ruberti, L. F. Deravi, *Chem* **2019**, *5*, 2126.
- [43] D. F. Mosher, R. B. Johnson, *J. Biol. Chem.* **1983**, *258*, 6595.
- [44] K. Sakai, T. Fujii, T. Hayashi, *J. Biochem.* **1994**, *115*, 415.
- [45] O. S. Ejim, G. W. Blunn, R. A. Brown, *Biomaterials* **1993**, *14*, 743.
- [46] R. Brown, G. Blunn, O. Ejim, *Biomaterials* **1994**, *15*, 457.
- [47] Z. Ahmed, S. Underwood, R. A. Brown, *Tissue Eng.* **2003**, *9*, 219.
- [48] S. Underwood, A. Afoke, R. A. Brown, A. J. MacLeod, P. A. Shamlou, P. Dunnill, *Biotechnol. Bioeng.* **2001**, *73*, 295.
- [49] N. Pernodet, M. Rafailovich, J. Sokolov, D. Xu, N.-L. Yang, K. McLeod, *J. Biomed. Mater. Res.* **2003**, *64A*, 684.
- [50] S. Ahn, L. F. Deravi, S.-J. Park, B. E. Dabiri, J.-S. Kim, K. K. Parker, K. Shin, *Adv. Mater.* **2015**, *27*, 2838.
- [51] A. W. Feinberg, K. K. Parker, *Nano Lett.* **2010**, *10*, 2184.
- [52] P. Rico, J. C. R. Hernández, D. Moratal, G. Altankov, M. M. Pradas, M. Salmerón-Sánchez, *Tissue Eng. Part A* **2009**, *15*, 3271.
- [53] S. Jordahl, L. Solorio, D. B. Neale, S. McDermott, J. H. Jordahl, A. Fox, C. Dunlay, A. Xiao, M. Brown, M. Wicha, G. D. Luker, J. Lahann, *Adv. Mater.* **2019**, *31*, 1904580.
- [54] G. Baneyx, V. Vogel, *Proc. Natl. Acad. Sci. USA* **1999**, *96*, 12518.
- [55] W. C. Little, M. L. Smith, U. Ebnetter, V. Vogel, *Matrix Biol.* **2008**, *27*, 451.
- [56] E. Klotzsch, M. L. Smith, K. E. Kubow, S. Muntwyler, W. C. Little, F. Beyeler, D. Gourdon, B. J. Nelson, V. Vogel, *Proc. Natl. Acad. Sci. USA* **2009**, *106*, 18267.
- [57] J. Ulmer, B. Geiger, J. P. Spatz, *Soft Matter* **2008**, *4*, 1998.
- [58] P. Kaiser, J. P. Spatz, *Soft Matter* **2010**, *6*, 113.
- [59] K. V. Nemani, K. L. Moodie, J. B. Brennick, A. Su, B. Gimi, *Mater. Sci. Eng. C* **2013**, *33*, 4453.
- [60] A. Shinde, S. Libring, A. Alpsoy, A. Abdullah, J. A. Schaber, L. Solorio, M. K. Wendt, *Mol. Cancer Res.* **2018**, *16*, 1579.
- [61] A. Shinde, J. S. Paez, S. Libring, K. Hopkins, L. Solorio, M. K. Wendt, *Oncogenesis* **2020**, *9*, 16.
- [62] P. H. Wu, D. M. Gilkes, D. Wirtz, *Annu. Rev. Biophys.* **2018**, *47*, 549.
- [63] B. A. Humphries, J. M. Buschhaus, Y.-C. Chen, H. R. Haley, T. Qyli, B. Chiang, N. Shen, S. Rajendran, A. Cutter, Y.-H. Cheng, Y.-T. Chen, J. Cong, P. C. Spinosa, E. Yoon, K. E. Luker, G. D. Luker, *Mol. Cancer Res.* **2019**, *17*, 1142.
- [64] K. Burrige, E. S. Wittchen, *J. Cell Biol.* **2013**, *200*, 9.
- [65] S. Pellegrin, H. Mellor, *J. Cell Sci.* **2007**, *120*, 3491.
- [66] N. E. Persson, J. Rafshoon, K. Naghshpour, T. Fast, P.-H. Chu, M. McBride, B. Risteen, M. Grover, E. Reichmanis, *ACS Appl. Mater. Interfaces* **2017**, *9*, 36090.
- [67] P.-H. Wu, A. Giri, D. Wirtz, *Nat. Protoc.* **2015**, *10*, 517.
- [68] P.-H. Wu, A. Giri, S. X. Sun, D. Wirtz, *Proc. Natl. Acad. Sci. USA* **2014**, *111*, 3949.
- [69] F. Ascione, A. Vasaturo, S. Caserta, V. D'Esposito, P. Formisano, S. Guido, *Exp. Cell Res.* **2016**, *347*, 123.
- [70] D. A. Lauffenburger, A. F. Horwitz, *Cell* **1996**, *84*, 359.
- [71] M. Krause, A. Gautreau, *Nat. Rev. Mol. Cell Biol.* **2014**, *15*, 577.
- [72] W. Y. Wang, C. D. Davidson, D. Lin, B. M. Baker, *Nat. Commun.* **2019**, *10*, 1186.
- [73] A. Shellard, R. Mayor, *Trends Cell Biol.* **2020**, *30*, 852.
- [74] J. S. Park, D. H. Kim, A. Levchenko, *Biophys. J.* **2018**, *114*, 1257.
- [75] J. Park, D.-H. Kim, H.-N. Kim, C. J. Wang, M. K. Kwak, E. Hur, K.-Y. Suh, S. S. An, A. Levchenko, *Nat. Mater.* **2016**, *15*, 792.
- [76] J. H. Jordahl, L. Solorio, H. Sun, S. Ramcharan, C. B. Teeple, H. R. Haley, K. J. Lee, T. W. Eyster, G. D. Luker, P. H. Krebsbach, J. Lahann, *Adv. Mater.* **2018**, *30*, 1707196.
- [77] F. M. Wunner, M.-L. Wille, T. G. Noonan, O. Bas, P. D. Dalton, E. M. De-Juan-Pardo, D. W. Huttmacher, *Adv. Mater.* **2018**, *30*, 1706570.
- [78] A. A. Szklanny, L. Debbi, U. Merdler, D. Neale, A. Muñoz, B. Kaplan, S. Guo, J. Lahann, S. Levenberg, *Adv. Funct. Mater.* **2020**, *30*, 1901335.